IEEE Access
Multidisciplinary | Rapid Review | Open Access Journal

Received 1 March 2024, accepted 29 March 2024, date of publication 9 April 2024, date of current version 23 April 2024.

Digital Object Identifier 10.1109/ACCESS.2024.3386761

RESEARCH ARTICLE

High Sensitivity Photon Pressure Sensitive Skin of Piercing Robot Based on Balloon-Shaped Fiber Optic Sensor

MENG JIAO CHI, HONG JUAN YANG, KUN SHAN YANG, WEI ZHUN DONG, XIN WEI WANG, SEN ZHANG, XI CHANG WANG, AND LING XIN KONG

Optical Fiber Based Intelligent Sensing and Micromachines Laboratory, Yantai University, Yantai 264005, China

Corresponding author: Hong Juan Yang (yanghongjuan123.hi@163.com)

This work was supported in part by the National Natural Science Foundation of China (NSFC) under Grant 62105278, in part by the Natural Science Foundation of Shandong Province under Grant ZR2021QF139, in part by the Doctoral Initiation Fund of Yantai University under Grant WL20B129 and Grant WL18B18, and in part by the Students Innovation and Entrepreneurship Training Program of Yantai University under Grant X202311066075.

ABSTRACT In this paper, a photonic skin sensor based on a balloon-shaped optical fiber structure cascading a Fiber Bragg Grating (FBG) is proposed, which can simultaneously sense pressure and temperature. When the photonic skin feels pressure, the built-in polymer micro-cap is squeezed, causing a change in the radius of the balloon-shaped structure. At the same time, the capillary-enclosed FBG can be used for temperature compensation. The pressure sensitivity of the photon skin sensor can reach 6.556 nm/mN in the range of 0-0.5 mN and the temperature sensitivity can reach −0.192 nm/°C in the range of 30-50 °C. The demodulation of the dual parameter matrix shows that the error rates of pressure and temperature measurements are less than 0.5% and 2.01%, respectively. On this basis, the sensor is applied to robotic arm-assisted puncture experiment detection, and the five states of the puncture process are analyzed. Based on the backpropagation (BP) neural network for repeated training, the results show that its accuracy remains at 98.7%, indicating that the sensor has good robustness. The development of this sensor shows application potential in the field of robotic intelligent skin in the future.

INDEX TERMS Balloon-shaped, pressure sensing, optical fiber, temperature sensing.

I. INTRODUCTION

Fiber optic sensing technology for robots has recently been a hot topic [1], [2]. Due to its small size, high sensitivity, and resistance to electromagnetic interference, it has more advantages in some particular environments. Among them, high-precision fiber optic force sensors have become one of the essential components of intelligent operating robots, which have been applied in industrial control, medical equipment, artificial intelligence, and other fields [3], [4], [5]. In 2020, Bai et al. presented a stretchable multimodal sensing photoconductive sensor, which can distinguish and measure the position, size, and mode of mechanical deformation of wearable gloves [6]. In 2022, Luca et al. developed a large area of sensitive soft skin based on fiber Bragg grating sensors. They decoded it using deep learning algorithms to infer the contact force's magnitude and the skin surface's location [7]. Therefore, developing fiber optic photonic skin will pave the way for intelligent robot perception.

Fiber Bragg grating is currently a commercial-grade fiber optic device, widely used in robot mechanical perception. However, its low strain sensitivity limits its application in high-precision measurement [8], [9], [10]. The measurement field of balloon-shaped fiber optic sensors is very extensive. In 2023, the balloon-shaped sensor made of graphite nitrite nanocomposites (g-C_3N_4/$ZrPO_4$) as a thin layer material was proposed. Nitrogen dioxide ions were detected by coating g-C_3N_4/$ZrPO_4$ nanocomposites on the flat part of spherical fibers, with a detection limit (LOD) of 182 ppb [11]. In the same year, in biomedicine, the reconfigurable and

The associate editor coordinating the review of this manuscript and approving it for publication was Sukhdev Roy.

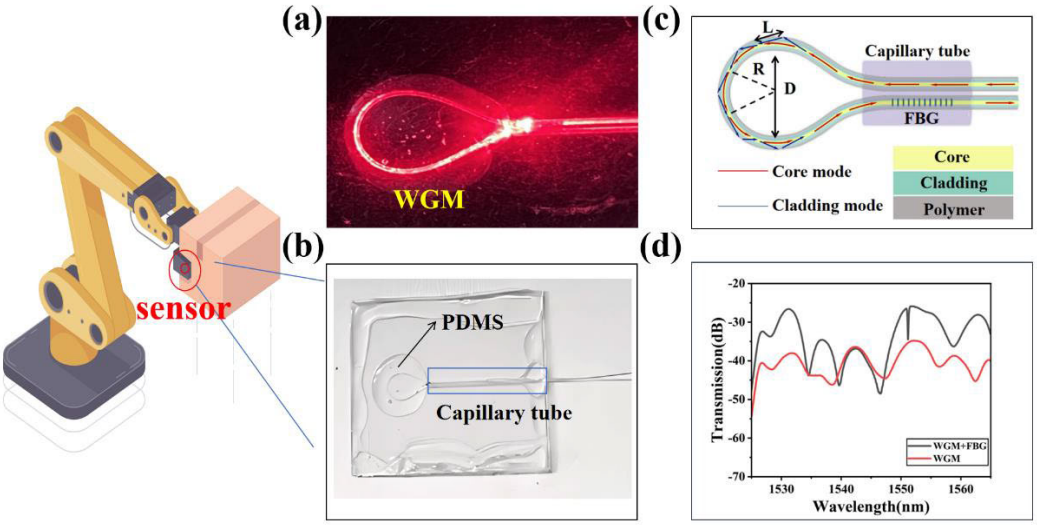

FIGURE 1. Application of fiber optic photon skin in grippers. (a) Microscopic photo of 660 nm wavelength light passing through the WGM sensor; (b) Physical image of sensor packaging; (c) Schematic diagram of the principle of fiber optic WGM sensor; (d) Transmission spectrum.

scalable balloon-shaped fiber wearable device was used for human pulse and respiratory monitoring [12]. Moreover, the balloon-shaped fiber optic sensor has the natural advantage of high sensitivity in force sensing and has potential research value in robot pressure sensing [13]. The effective refractive index (RI) and length of balloon-shaped fiber optic sensors change during force, leading to light intensity or spectral drift changes, making them suitable for high-sensitivity mechanical detection in small spaces. In recent years, deep learning has received widespread attention in fiber optic sensing to improve the accuracy and stability of robot perception effectively [14], [15].

This article proposes a fiber optic photon skin sensor based on deep learning. The balloon-shaped structure is used for pressure sensing, and FBG is used for temperature compensation. This article calibrates the cross-response of sensors under different pressures and temperatures. The pressure sensitivity can reach 6.556 nm/mN in the 0-0.5 mN range, and the temperature sensitivity can reach 0.192 nm/°C in the 30-50 °C range. The sensor is applied to the state detection of the puncture robotic arm, and repeated training is conducted based on the BP neural network. The results verify that the sensor has good robustness. This sensor has potential application prospects in strain and temperature sensing of robots.

II. STRUCTURE AND PRINCIPLE

The schematic diagram of the sensor applied to the robotic arm is shown in Fig. 1. The sensor consists of a balloon-shaped single-mode fiber (SMF) based on Whispering Gallery Mode (WGM) and an FBG with a central wavelength of 1551 nm. Fig. 1(a) shows a physical photo of red light passing through a balloon-shaped sensor. The overall structure diagram of the encapsulated sensor is shown in Fig. 1(b). The balloon-shaped structure is placed on a polymer micro-cap with the advantages of the high Poisson's ratio coefficient and the low Young's modulus. Thus, the sensor shows a high sensitivity to a weak change in pressure [5]. The pressure or temperature changes can cause deformation of the polymer micro-cap, thereby causing deformation of the balloon-shaped fiber optic sensing structure. The schematic diagram of the fiber optic sensor is shown in Fig. 1(c). The bending diameter of the balloon structure is D, with R as the center radius. Fig. 1(d) shows the transmission spectrum of the composite sensor, including WGM spectrum (Dip-1) and FBG spectrum (Dip-2). It can be seen that the spectra of the composite sensor are superimposed of the spectra of the balloon-shaped structure and the FBG. The differences in resonance wavelength of WGM between the two spectra are due that the spectra are recorded without the polymer micro-cap and the UV glue.

The schematic diagram of the sensor structure is shown in Fig. 2, which mainly includes structure preparation and pack–aging. Firstly, a section of SMF was bent into a balloon-shaped by mechanical folding method. Then it was connected with an FBG. The FBG is encapsulated in a hollow glass tube with an inner diameter of 400 μm. Secondly, the glass tube was sealed with UV glue, which is used to protect the FBG. Thirdly, a polymer micro-cap was made on the bottom acrylic pressure plate. Then the sensor was placed on the micro-cap, and the upper acrylic pressure plate was covered on it. Finally, the entire structure was cured and encapsulated with UV glue. The coating layer of the optical fiber has not been removed to ensure minimal spectral loss and protect the fiber optic structure.

The operating principle of the sensor is based on the interference between the fiber core mode and the whispering gallery mode. When the angle of incidence is larger than the critical angle, the light is totally reflected at the interface between the cladding and the air, forming the whispering gallery mode. Subsequently, the core mode and the whispering gallery mode form a double-beam interference. The

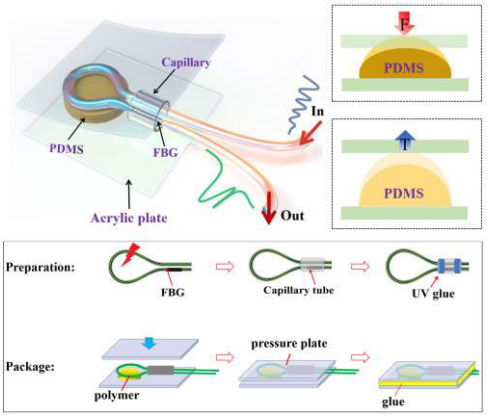

FIGURE 2. Schematic diagram of the sensor preparation process.

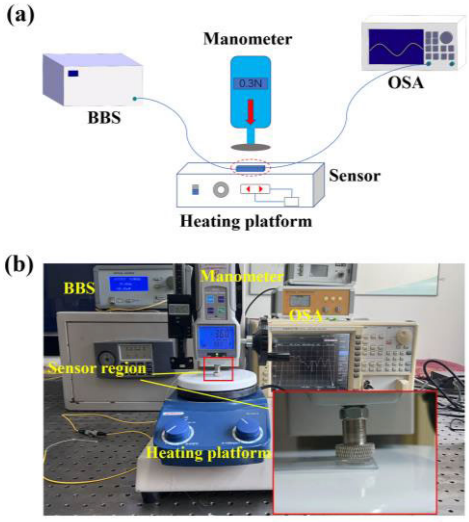

FIGURE 3. Experimental system setup. (a) Schematic diagram of the experimental setup; (b) Physical diagram of the experimental setup.

resulting transmission intensity in the transmission spectrum can be expressed as [16]

$$I_{out} = I_{core} + I_{m,WGM} + 2\sqrt{I_{core} I_{m,WGM}}\, cos\, \frac{2\pi L_{eff}\, \Delta n_{eff}}{\lambda} \tag{1}$$

where I_{core} and $I_{m,WGM}$ are the intensity of the core mode and m-order cladding whispering gallery mode respectively. λ is the wavelength in the air, L_{eff} is the effective optical path length of the bent region. Δn_{eff} is the difference between the effective RI of the core mode and the effective RI of the m-order whisper gallery mode, expressed as

$$\Delta n_{eff} = n_{core}^{eff} - n_{m,WGM}^{eff} \tag{2}$$

where n_{core}^{eff} is the effective RI of the core mode, $n_{m,WGM}^{eff}$ is the effective RI of the m-order whisper gallery mode. $\frac{2\pi L_{eff}\, \Delta n_{eff}}{\lambda} = (2m+1)\pi$ is phase difference of the fiber core mode and WGM, where m is a positive integer that can take values of 0, 1, 2.... When the phase difference is 2mπ, the intensity is enhanced, corresponding to the position of the resonance peak. When the phase difference is (2m+1) π, the intensity is weakened, corresponding to the position of the resonance dip. The interference light resonance dip wavelength (λ_{WGM}) appears at a specific wavelength, which can be expressed as [16]

$$\lambda_{WGM} = \frac{2L_{eff}}{2m+1} \cdot \Delta n_{eff} \tag{3}$$

From (3), it can be seen that the wavelength of the WGM structure will be affected by L_{eff} and Δn_{eff}, and different wavelengths are independent with each other. When the temperature is constant, the effective RI of the sensor is almost constant, then the WGM structure wavelength will only be changed by the pressure-induced change in the effective optical path length L. The fiber RI change can be approximately neglected compared to the L change due to deformation. Therefore, the sensitivity of the WGM structure can be expressed as

$$\begin{aligned} K_{WGM} &= \frac{\partial \lambda}{\partial D_{P,T}} \\ &= \frac{2}{2k+1} \cdot \left(\frac{\partial L_{eff}}{\partial D_{P,T}} \cdot \Delta n_{eff} + \frac{\partial \Delta n_{eff}}{\partial D_{P,T}} \cdot L_{eff} \right) \end{aligned} \tag{4}$$

The central wavelength of the FBG can be expressed as [17]

$$\lambda_{FBG} = 2 n_{eff}^{core} \Lambda \tag{5}$$

where Λ is the period of the FBG. Changes in temperature or when a force is applied to the FBG can lead to changes in the effective RI and grating period of the fiber. The measurement of the FBG for the pressure is essentially obtained by the detection of the strain, assuming that the rest of the external physical quantities remain unchanged and that the FBG is only affected by a uniform positive pressure P, then the pressure sensitivity and temperature sensitivity of the FBG structure can be expressed respectively as [17]

$$K_{P,FBG} = \frac{\partial \lambda_B}{\partial P} = \lambda_B (1 - P_e) \tag{6}$$

$$K_{T,FBG} = \frac{\partial \lambda_B}{\partial T} = \lambda_B (\alpha + \zeta) \tag{7}$$

where P_e is the effective elastic coefficient of optical fiber, α is the thermal expansion coefficient of optical fiber and ζ is the thermal optic coefficient of optical fiber.

With the variety of pressure and temperature simultaneously, the wavelength shifts of the WGM and FBG inclinations can be expressed by the sensitivity matrix as [18]

$$\begin{bmatrix} \Delta\lambda_{WGM} \\ \Delta\lambda_{FBG} \end{bmatrix} = \begin{bmatrix} K_{P,WGM} & K_{T,WGM} \\ K_{P,FBG} & K_{T,FBG} \end{bmatrix} \begin{bmatrix} \Delta P \\ \Delta T \end{bmatrix} \tag{8}$$

The two-parameter measurement is implemented by the inverse matrix with its mathematical expression:

$$\begin{bmatrix} \Delta P \\ \Delta T \end{bmatrix} = \begin{bmatrix} K_{P,WGM} & K_{T,WGM} \\ K_{P,FBG} & K_{T,FBG} \end{bmatrix}^{-1} \begin{bmatrix} \Delta\lambda_{WGM} \\ \Delta\lambda_{FBG} \end{bmatrix} \tag{9}$$

where $K_{P,WGM}$ and $K_{T,WGM}$ are the pressure and temperature sensitivity coefficients of the whispering gallery structure, respectively. $K_{P,FBG}$ and $K_{T,FBG}$ are the pressure

and temperature sensitivity coefficients of the FBG structure, respectively. ΔP is the amount of pressure change, ΔT is the amount of temperature change. The actual temperature and pressure changes can be obtained through calculation, so as to realize the simultaneous measurement of both and solve the problem of cross-sensitivity.

III. EXPERIMENTS AND RESULTS

A. SYSTEM CONSTRUCTION AND PARAMETER OPTIMIZATION

The experimental setup for testing the pressure and temperature characteristics of the sensor is shown in Fig. 3. The packaged sensor is placed horizontally on a heated platform (SH-II-8B, 0-400 °C), and above the sensor is a test stand (HLD with scale) and a vertically suspended manometer (SP-2, 0-2 N). The resolution of the manometer is 0.0001 N. The sensor connects to a broadband light source (BBS, 1525-1575 nm) and a spectrometer (OSA, AQ6370, 600-1700 nm) on both sides, and the output spectral wavelength drift is recorded by OSA. The lowest temperature setting of the heating platform has a resolution of 0.1 °C.

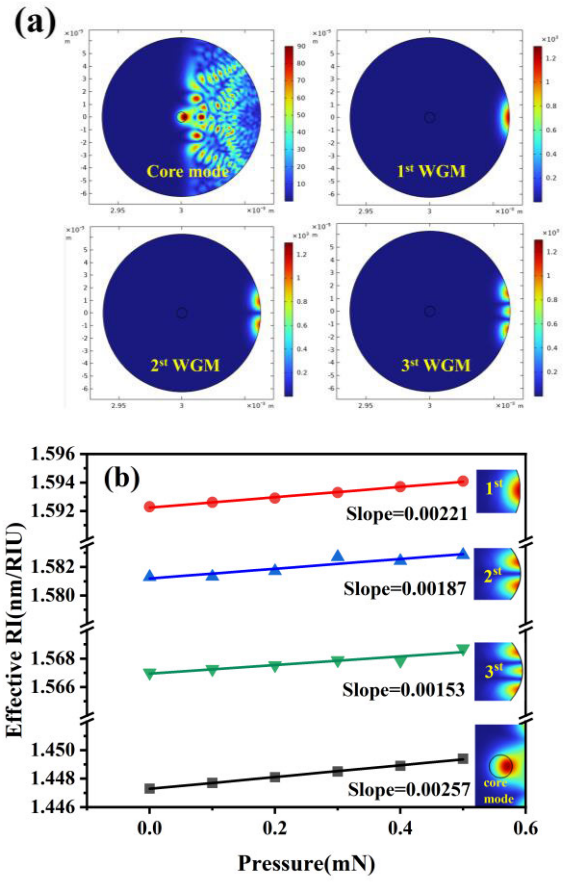

FIGURE 4. (a) Modal fields analysis with the bending diameter of 6 mm; (b) Effective refractive index change of the mode.

The bending diameter of the balloon-shaped structure is an important parameter that affects the performance of the sensor. In order to study the effect of the bending diameter on the sensing structure, the finite element method is used to analyze the mode field diagrams of the whispering gallery mode of the curved waveguide. The research results indicate that the interference between the core mode and higher-order mode is mainly stimulated. Fig. 4 (a) shows the modal field diagrams of the core mode and the 1st, 2nd, and 3rd order cladding modes.

Due to the existence of the elasto-optical effect, the dielectric constant can be increase with stress applying to the balloon-shaped structure. Thus, the effective RI can be changed accordingly. When the pressure applied to the sensor changes, the effective RI of the four modes listed in Fig. 4 (a) varies with the surrounding pressure, as shown in Fig. 4 (b). It can be seen that the effective RI of the cladding mode is higher than that of the core mode, and the effective RI of each mode increases with the increase of pressure. The RI growth rate of the core mode is higher than that of any cladding mode. Therefore $\Delta n_{eff} > 0$. From (3), it can be seen that as the pressure increases, the interference spectrum will shift towards longer wavelengths.

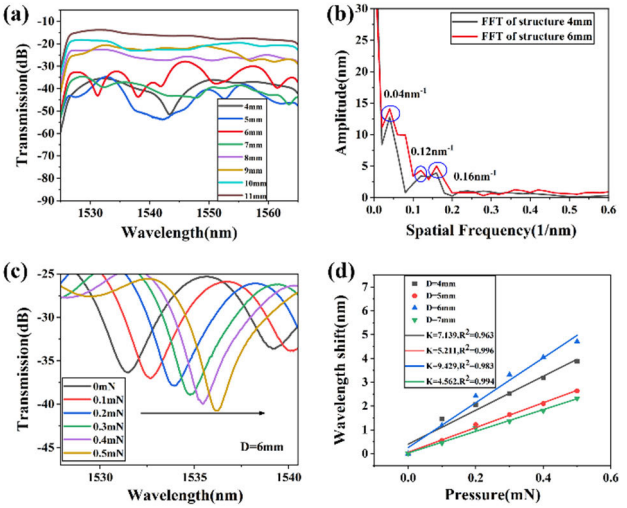

FIGURE 5. (a) Sensing structures with different bending diameters; (b) Fourier analysis; (c) Experimental spectrum with a bending diameter of 6 mm; (d) The fitted pressure sensitivity of different structures.

This article introduces eight sensors with different bending diameters (D=4 mm, 5 mm, 6 mm, 7 mm, 8 mm, 9 mm, 10 mm, 11 mm) for experimental research, as shown in Fig. 5(a). The experimental results indicate good interference spectra occur when the bending diameters are 4 mm, 5 mm, and 6 mm. When the bending diameter is 7mm, 8mm, 9mm, 10mm, and 11mm, interference dip with good contrast cannot be detected in the transmission spectrum. This is due to the bending diameter being too large, causing a small amount of light to leak from the fiber core into the cladding, resulting in low visibility of interference fringes and the inability to achieve coupling between the fiber core and cladding. When the bending diameters are 4 mm and 5 mm respectively, although interference fringes can be detected, the free spectral range is too large and it is not easy to have a suitable dip near the central wavelength of the FBG. Therefore, sensors with 4 mm diameter and 5 mm diameter are not selected

for subsequent experiments. As the bending radius decreases, more light intensity escapes into the cladding and leaks out of the SMF, resulting in a large signal loss and reduced spectral intensity.

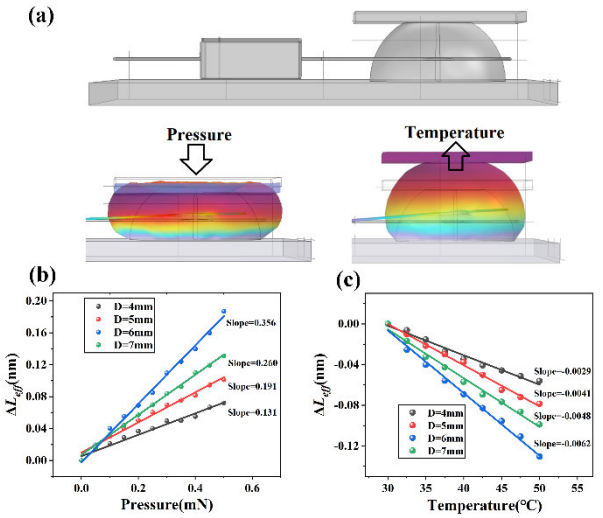

FIGURE 6. Structural Simulation Analysis. (a) Pressure die-field diagram simulation and Temperature die-field diagram simulation; (b) Linear relationship between ΔL_{eff} and pressure; (c) Linear relationship between ΔL_{eff} and temperature.

In order to further investigate the sensing characteristics of sensors with bending diameters of 4 mm and 6 mm, we use the Fast Fourier Transform (FFT) to analyze their interference spectra in the spatial frequency domain, as shown in Fig. 5(b). The results indicate that the spatial spectrum is dominated by dominant enormously excited envelope modes, consistent with theoretical analysis. Four types of sensors with different structures are encapsulated and pressure experiments are conducted at room temperature. The experimental results are shown in Fig. 5(c). With the increased pressure applied, the transmission spectra are shifted to the long wavelength side, and the experimental results agree with the theoretical analysis above. Since the experimental results of 5 mm and 7 mm are unsatisfactory, the average pressure sensitivity is obtained through repeated experiments. Finally, the pressure sensitivity of the four structures is fitted, as shown in Fig. 5(d). The experimental results demonstrate that the pressure sensitivity of structures with a bending diameter of 4 mm is lower than that of structures with a bending diameter of 6 mm. At the same time, the smaller diameter of the optical fiber causes excessive prestress in the balloon-shaped sensor, making it prone to breakage. Therefore, package the sensor structure with a bending diameter of 6 mm and conduct application-oriented experiments.

B. EXPERIMENT ANALYSIS

Since the L_{eff} is changed in the spatial dimension, the spherical structure is simulated using the finite element method and the results are shown in Fig. 6. When the pressure and temperature are changed, ΔL_{eff} undergoes a downward and upward shift in the spatial dimension, respectively. The calculations show that ΔL_{eff} increases in a linear trend as the applied pressure increases, and ΔL_{eff} decreases linearly with increasing temperature.

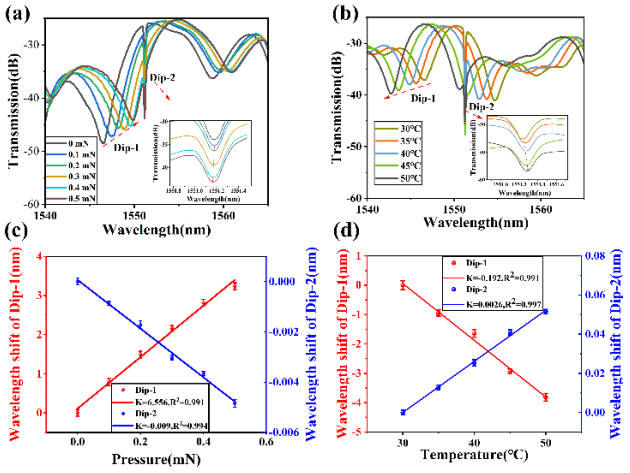

FIGURE 7. (a) The experimental spectrum at different pressures. Inset: The experimental spectrum of Dip-2; (b) The experimental spectra at different temperatures. Inset: The experimental spectrum of Dip-2; (c) Sensitivity fitting lines under different pressures; (d) Sensitivity fitting lines under different temperatures.

Owing to investigate the effect of pressure on the wavelength drift of the balloon-shaped sensor, under the condition of constant temperature and the pressure measurement range of 0-0.5 mN, apply 0.1 mN of pressure to the sensor each time and record the stable transmission spectra. The results are shown in Fig. 7(a). It can be seen that the characteristic wavelength Dip-1 of the WGM structure has undergone a redshift, which is due to the excellent tensile resilience of the cured PDMS. The sensor undergoes deformation due to pressure compression, causing a change in the optical path length of the whispering gallery mode, which grows the characteristic wavelength. The pressure sensitivity of the characteristic wavelength Dip-1 can reach 6.556 nm/mN. However, the characteristic wavelength Dip-2 is extremely insensitive to pressure and undergoes a slight blue shift, with a pressure sensitivity of −0.009 nm/mN, as shown in Fig. 7(c).

The packed sensor is placed horizontally on the heating platform without applying any pressure. During the temperature experiment, the initial temperature is set to 30 °C, and the transmission spectrum is recorded every five °C, with the temperature range set from 30 °C to 50 °C. At each temperature recording point, the temperature is kept constant, and the data are recorded after 5 min to avoid the contingency caused by the experiment. The experimental results are shown in Fig. 7(b). As the ambient temperature increases, the characteristic wavelength Dip-1 of the WGM structure undergoes a blue shift due to the thermal expansion of the polymer PDMS and volume becoming larger, resulting in a smaller characteristic wavelength λ. The temperature sensitivity can reach −0.192 nm/°C, while Dip-2 undergoes a redshift with a temperature sensitivity of 0.0026 nm/°C, as shown in Fig. 7(d). This phenomenon indicates that Dip-1

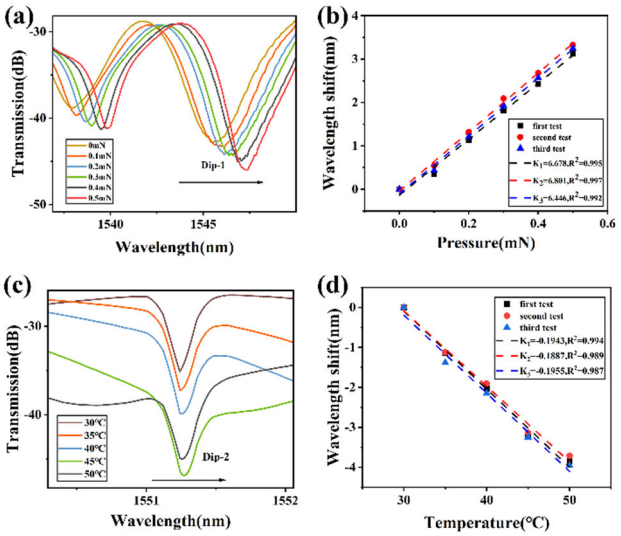

FIGURE 8. Repetitive experimental results of the sensor. (a) The enlarged spectrum of Dip-1; (b) Linear fitting diagram of the three experiments of Dip-1; (c) The enlarged spectrum of Dip-2; (d) Linear fitting diagram of the three experiments of Dip-2.

and Dip-2 are both temperature sensitive, and compared to Dip-1, Dip-2 has lower temperature sensitivity. Therefore, temperature compensation can be achieved through dual-parameter demodulation.

During the experiment, in order to verify the repeatability of the sensor, we conducted repeated experiments on the sensor every three days under the same conditions. The three measurement spectra of the same sensor are shown in Fig. 8. The magnified spectrum of Dip-1 is shown in Fig. 8(a). The linear fitting curves of wavelength drift corresponding to the three experiments of Dip-1 are shown in Fig. 8(b), with corresponding sensitivities of 6.678, 6.801, and 6.446, and relative errors of 1.3%. The magnified spectrum of Dip-2 is shown in Fig. 8(c), and the linear fitting curve of wavelength drift corresponding to the three experiments of Dip-2 is shown in Fig. 8(d). The corresponding sensitivities are −0.1829, −0.1877, −0.1955, and the relative error is −1.71%.

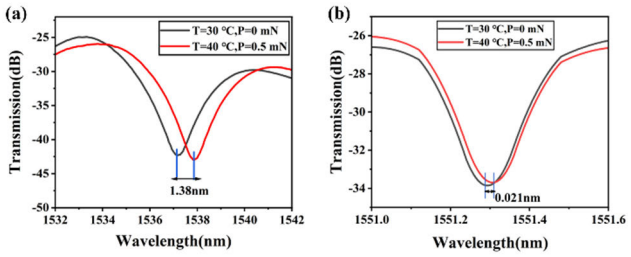

FIGURE 9. (a) Experimental spectral variation of Dip-1; (b) Experimental spectral variation of Dip-2.

C. ERROR ANALYSIS

Finally, the temperature (30-40 °C) and the pressure (0-0.5 mN) are varied simultaneously. The actual change of the two parameters is $\Delta P = 0.5$ mN, $\Delta T = 10$ °C. As shown in Fig. 9(a), the data obtained from the experimental spectra are: $\Delta\lambda_{Dip-1} = 1.38$ nm, $\Delta\lambda_{Dip-2} = 0.021$ nm, as shown in Fig. 9(b).

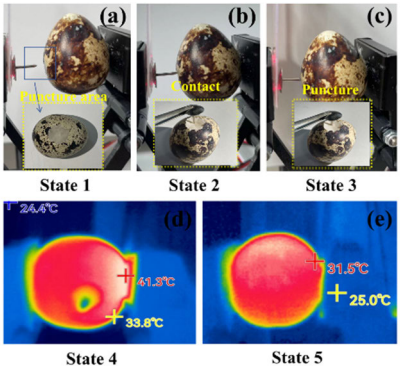

FIGURE 10. The critical state of the puncture process. (a) non-contact state at 30 °C; (b) Contact state at 30 °C; (c) Rupture state at 30 °C; (d) Infrared imaging image at 41.3 °C; (e) Infrared imaging image at 31.5 °C.

According to the above experimental analysis, (10) can be expressed as:

$$\begin{bmatrix} \Delta P \\ \Delta T \end{bmatrix} = \frac{1}{65.2844} \begin{bmatrix} 0.0026 & 0.192 \\ 0.009 & 6.556 \end{bmatrix} \begin{bmatrix} 1.38 \\ 0.021 \end{bmatrix} \tag{10}$$

The solution matrix obtains the values of two variables: $\Delta P = 0.4975$ mN, $\Delta T = 9.7989$ °C. Calculated error rate: $E(\Delta P) = 0.5$ %, $E(\Delta T) = 2.01$%.

IV. APPLICATION TESTS

Percutaneous perforation has critical clinical applications in diagnosing and treating diseased tissue biopsy, ablation, and radiotherapy [23], [24], [25]. Robots are widely used for robotic-assisted puncture procedures due to their high dexterity and precision [26], [27]. Therefore, the eggshell membrane is used to simulate human surface skin, and a puncture surgery system is constructed, installing the sensor and needles on the inner side of the robotic arm. This system can calculate the puncture force by monitoring wavelength drift and sensing the position of needles during the puncture process. During the puncture process, the range of puncture force is calculated by monitoring the critical state of the eggshell membrane.

The three critical states of the puncture process are analyzed in detail: non-contact state, the contacted state, and the punctured state, as shown in Fig. 10(a), (b) and (c). By monitoring wavelength drift in real time, spectral change maps of three states are obtained, as shown in Fig. 11(a) and (b). The wavelength shift of the contact state is 1.34 nm, while the wavelength shift of the puncture state is 5.48 nm. By introducing a demodulation matrix, the pressure range obtained is 0.1099-0.6168 mN, and the actual pressure range of the pressure gauge is 0-0.5 mN. Therefore, a pressure error of 1.38% can be calculated. Fig. 10(d) and (e) show the actual temperature measured. Considering the temperature interference during the puncture process, it is necessary to use matrix

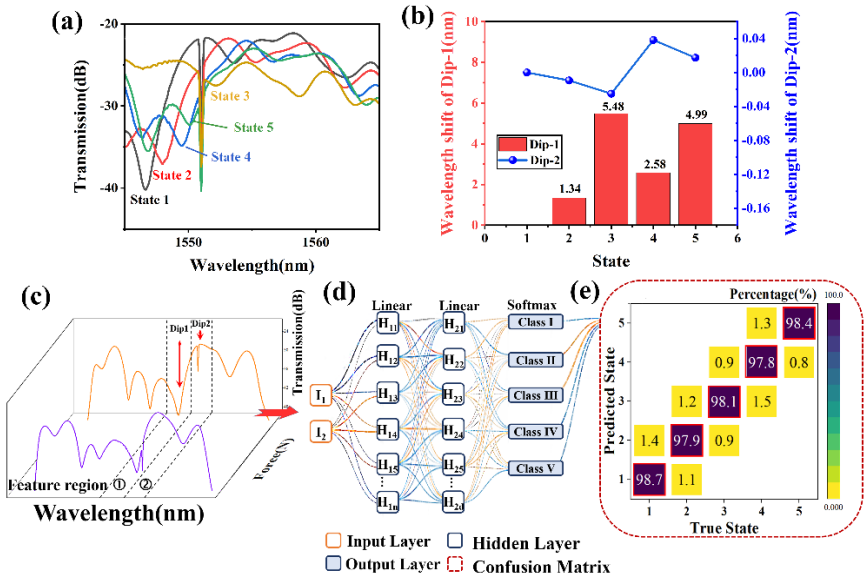

FIGURE 11. Analyze the five states of the puncture process and the BP neural network demodulation scheme. (a) Spectra of the five states of the puncture process; (b) Wavelength shift of the five states of the puncture process; (c) Extracted spectral features; (d) Schematic view of demodulation scheme based on BP model; (e) Confusion matrix with the highest accuracy of 98.7% for the state recognition.

demodulation. In minimally invasive surgery (MIS), robot-assisted puncture provides important guarantees for smooth pathological detection and minimally invasive surgery of patients.

The variations in the spectrum are too minor to capture the critical state in time for practical applications. Therefore, backward propagation (BP) neural network is used to solve this problem. Usually, supervised machine learning methods require a dataset for training. Therefore, we collect a dataset containing force and temperature features in five critical states. As shown in Fig. 10(c), we extract the region containing characteristic dips of force and temperature in the spectrum, respectively, and preprocess it for training the BP network model. The BP neural network is a classical multilayer perceptron, which can effectively approximate the continuous function to be fitted by forward propagation of data and backward propagation of error [28], [29], [30]. In Fig. 10(d), the structure of the BP neural network used in this paper is 2-30-30-5, where the input layer has 2 neurons, which is equal to the dimensionality of the features in the spectrum. The hidden layer 1 has 30 neurons, the hidden layer 2 has 30 neurons, and the output layer has 5 neurons, which represent the five critical states mentioned above. The confusion matrix in Fig. 10(e) achieves the highest accuracy of 98.7%. The misjudgments may be attributed to the instability of the spectral data and the structural changes in the target's skin. The misjudgment error is less than 1.4%, which shows the ability to expand the application of photonic skin sensors in biochemical and robotic sensing.

To verify the accuracy of BP neural network results, the experiment with the temperature range of 30-39 °C every 0.5 °C was proceeded, as shown in Fig. 12(a). The 19 sets of temperature spectral data are collected and labeled with 19 different labels for the training and validation process of the model. The confusion matrix of the test results is shown in Fig. 12(b), where the horizontal axis represents the true label of the temperature data, the vertical axis represents the label predicted by the neural network for the temperature data, and the numbers in the figure represent the predicted probabilities of different categories of temperature. According to the confusion matrix, the prediction accuracy of the model for different temperatures remains above 97% despite the small probability of prediction error in the adjacent data. It shows that the use of neural networks can well classify the output spectra of optical fibers under different temperature conditions and can further improve the sensing performance of the sensors proposed in this paper.

Compared with other two-parameter optical fiber force sensors, this work has excellent performance indicators, as shown in Table 1. The results show that the sensor is susceptible and has unique advantages regarding temperature compensation.

TABLE 1. Compared with other optical fiber Force sensors.

Sensor structure	Force sensitivity (nm/mN)	Temperature sensitivity (nm/°C)	Reference
LPG	-0.00218	0.0086	[19]
Fabry–Perot cavity	0.0142	0.0004	[20]
multi-parameter FBG	0.0033	0.009	[21]
FP micro-cavity plugged by cantilever taper	0.842	0.011	[22]
WGM-FBG interferometer	6.556	0.192	This work

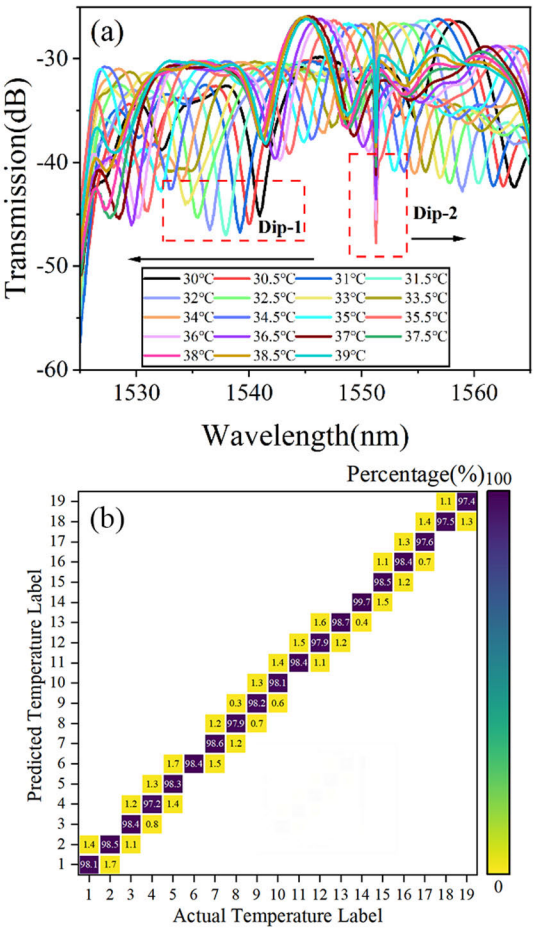

FIGURE 12. **(a) Spectral graphs of 19 temperature states; (b) Confusion matrix for the temperature recognition.**

V. CONCLUSION

This article proposes and designs a fiber optic photonic skin sensor with a built-in polymer micro-cap, which achieves simultaneous sensing of pressure and temperature. By calibrating the cross response of the sensor under different pressures and temperatures, it is found that its pressure sensitivity is as high as 6.556 nm/mN in the range of 0-0.5 mN. In addition, we use machine learning methods to verify that the sensor has good robustness, with an average recognition accuracy of 98.7%. By simply replacing polymer materials, this structure can be easily extended to measure other biochemical parameters. Compared with other optical fiber force sensors, this highly sensitive photon skin pressure sensors can be used in a small pressure range. Therefore, this sensor can be applied in high-precision and small-scale measurement fields such as MIS.

REFERENCES

[1] O. A. Araromi, M. A. Graule, K. L. Dorsey, S. Castellanos, J. R. Foster, W.-H. Hsu, A. E. Passy, J. J. Vlassak, J. C. Weaver, C. J. Walsh, and R. J. Wood, "Ultra-sensitive and resilient compliant strain gauges for soft machines," *Nature*, vol. 587, no. 7833, pp. 219–224, Nov. 2020, doi: 10.1038/s41586-020-2892-6.

[2] W. Lai, L. Cao, J. Liu, S. Chuan Tjin, and S. J. Phee, "A three-axial force sensor based on fiber Bragg gratings for surgical robots," *IEEE/ASME Trans. Mechatronics*, vol. 27, no. 2, pp. 777–789, Apr. 2022, doi: 10.1109/TMECH.2021.3071437.

[3] Y. Yao, M. Yan, and Y. Bao, "Measurement of cable forces for automated monitoring of engineering structures using fiber optic sensors: A review," *Autom. Construct.*, vol. 126, Jun. 2021, Art. no. 103687, doi: 10.1016/j.autcon.2021.103687.

[4] Y. Deng, T. Yang, S. Dai, and G. Song, "A miniature triaxial fiber optic force sensor for flexible ureteroscopy," *IEEE Trans. Biomed. Eng.*, vol. 68, no. 8, pp. 2339–2347, Aug. 2021, doi: 10.1109/TBME.2020.3034336.

[5] M. Q. Zou, C. R. Liao, S. Liu, C. Xiong, C. Zhao, J. L. Zhao, Z. S. Gan, Y. P. Chen, K. M. Yang, D. Liu, Y. Wang, and Y. P. Wang, "Fiber-tip polymer clamped-beam probe for high-sensitivity nanoforce measurements," *Light: Sci. Appl.*, vol. 10, p. 171, Aug. 2021, doi: 10.1038/s41377-021-00611-9.

[6] H. Bai, S. Li, J. Barreiros, Y. Tu, C. R. Pollock, and R. F. Shepherd, "Stretchable distributed fiber-optic sensors," *Science*, vol. 370, no. 6518, pp. 848–852, Nov. 2020, doi: 10.1126/science.aba5504.

[7] L. Massari, G. Fransvea, J. D'Abbraccio, M. Filosa, G. Terruso, A. Aliperta, G. D'Alesio, M. Zaltieri, E. Schena, E. Palermo, E. Sinibaldi, and C. M. Oddo, "Functional mimicry of Ruffini receptors with fibre Bragg gratings and deep neural networks enables a bio-inspired large-area tactile-sensitive skin," *Nature Mach. Intell.*, vol. 4, no. 5, pp. 425–435, May 2022, doi: 10.1038/s42256-022-00487-3.

[8] M. A. Butt, N. L. Kazanskiy, and S. N. Khonina, "Advances in waveguide Bragg grating structures, platforms, and applications: An up-to-date appraisal," *Biosensors*, vol. 12, no. 7, p. 497, Jul. 2022, doi: 10.3390/bios12070497.

[9] F. Mashayekhi, J. Bardon, Y. Koutsawa, S. Westermann, and F. Addiego, "Methods for embedding fiber Bragg grating sensors during material extrusion: Relationship between the interfacial bonding and strain transfer," *Additive Manuf.*, vol. 68, Apr. 2023, Art. no. 103497, doi: 10.1016/j.addma.2023.103497.

[10] R. You, L. Ren, and G. Song, "A novel fiber Bragg grating (FBG) soil strain sensor," *Measurement*, vol. 139, pp. 85–91, Jun. 2019, doi: 10.1016/j.measurement.2019.03.007.

[11] S. K. Swain, S. K. Majhi, M. Mishra, G. Phaomei, N. K. Sahoo, and S. K. Tripathy, "A new design of a fiber optic sensor based on balloon shaped bending and flattening sensing probe: Application towards an ultra specific and sensitive detection of nitrite using g-C_3N_4/$ZrPO_4$ nanocomposites coating," *Opt. Fiber Technol.*, vol. 81, Dec. 2023, Art. no. 103518, doi: 10.1016/j.yofte.2023.103518.

[12] Y. Wu, S. Xiao, Y. Xu, Y. Shen, Y. Jiang, W. Jin, Y. Yang, and S. Jian, "Highly sensitive force sensor based on balloon-like interferometer," *Opt. Laser Technol.*, vol. 103, pp. 17–21, Jul. 2018, doi: 10.1016/j.optlastec.2018.01.008.

[13] P. Mishra, P. K. Sahu, H. Kumar, and R. Jha, "Human pulse and respiration monitoring: Reconfigurable and scalable balloon-shaped fiber wearables," *Adv. Mater. Technol.*, vol. 8, no. 17, 2023, Art. no. 2300429, doi: 10.1002/admt.202300429.

[14] W. Z. Heng, S. Solomon, and W. Gao, "Flexible electronics and devices as human–machine interfaces for medical robotics," *Adv. Mater.*, vol. 34, no. 16, 2022, Art. no. 2107902, doi: 10.1002/adma.202107902.

[15] S. Pyo, J. Lee, K. Bae, S. Sim, and J. Kim, "Recent progress in flexible tactile sensors for human-interactive systems: From sensors to advanced applications," *Adv. Mater.*, vol. 33, no. 47, 2021, Art. no. 2005902, doi: 10.1002/adma.202005902.

[16] L. Cai, X. Ai, and Y. Zhao, "A displacement sensor based on balloon-like optical fiber structure," *Sens. Actuators A, Phys.*, vol. 338, May 2022, Art. no. 113469, doi: 10.1016/j.sna.2022.113469.

[17] M. Liu, W. Wang, H. Song, S. Zhou, and W. Zhou, "A high sensitivity FBG strain sensor based on flexible Hinge," *Sensors*, vol. 19, no. 8, p. 1931, Apr. 2019, doi: 10.3390/s19081931.

[18] X. Wang, J. F. Jiang, S. H. Wang, K. Liu, and T. G. Liu, "All-silicon dual-cavity fiber-optic pressure sensor with ultralow pressure-temperature cross-sensitivity and wide working temperature range," *Photon. Res.*, vol. 9, no. 4, pp. 521–529, 2021, doi: 10.1364/PRJ.414121.

[19] J. B. Xu, Y. G. Liu, Z. Wang, and B. Y. Tai, "Simultaneous force and temperature measurement using long-period grating written on the joint of a microstructured optical fiber and a single mode fiber," *Appl. Opt.*, vol. 49, no. 3, pp. 492–496, 2010, doi: 10.1364/ao.49.000492.

[20] J. N. Dash, Z. Y. Liu, D. S. Gunawardena, and H. Y. Tam, "Fabry–Pérot cavity-based contact force sensor with high precision and a broad operational range," *Opt. Lett.*, vol. 44, no. 14, pp. 3546–3549, 2019, doi: 10.1364/OL.44.003546.
[21] B. Hopf, F. J. Dutz, T. Bosselmann, M. Willsch, A. W. Koch, and J. Roths, "Iterative matrix algorithm for high precision temperature and force decoupling in multi-parameter FBG sensing," *Opt. Exp.*, vol. 26, no. 9, pp. 12092–12105, 2018, doi: 10.1364/oe.26.012092.
[22] Y. Liu, C. P. Lang, X. C. Wei, and S. L. Qu, "Strain force sensor with ultra-high sensitivity based on fiber inline Fabry–Pérot micro-cavity plugged by cantilever taper," *Opt. Exp.*, vol. 25, no. 7, pp. 7797–7806, 2017, doi: 10.1364/OE.25.007797.
[23] R. P. Krishna, R. K. Singh, A. Behari, A. Kumar, R. Saxena, and V. K. Kapoor, "Post-endoscopic retrograde cholangiopancreatography perforation managed by surgery or percutaneous drainage," *Surgery Today*, vol. 41, no. 5, pp. 660–666, May 2011, doi: 10.1007/s00595-009-4331-z.
[24] F. Akbulut, A. Tok, N. Penbegul, M. Daggulli, B. Eryildirim, S. Adanur, G. Gurbuz, H. Celik, M. M. Utangac, O. Dede, M. N. Bodakci, A. Tepeler, and K. Sarica, "Colon perforation related to percutaneous nephrolithotomy: From diagnosis to treatment," *Urolithiasis*, vol. 43, no. 6, pp. 521–526, Nov. 2015, doi: 10.1007/s00240-015-0792-2.
[25] P. Dibba, E. Ludwig, D. Calo, H. Gerdes, A. Markowitz, M. Shike, M. Schattner, and R. Mendelsohn, "Bevacizumab does not increase risk of perforation in patients undergoing percutaneous endoscopic gastrostomy or jejunostomy placement," *Surgical Endoscopy*, vol. 35, pp. 2976–2980, Jun. 2021, doi: 10.1016/j.gie.2015.03.002.
[26] N. Hungr, I. Bricault, P. Cinquin, and C. Fouard, "Design and validation of a CT- and MRI-guided robot for percutaneous needle procedures," *IEEE Trans. Robot.*, vol. 32, no. 4, pp. 973–987, Aug. 2016, doi: 10.1118/1.4955174.
[27] T. Hiraki, T. Kamegawa, T. Matsuno, T. Komaki, J. Sakurai, and S. Kanazawa, "Zerobot: A remote-controlled robot for needle insertion in CT-guided interventional radiology developed at Okayama University," *Acta Medica Okayama*, vol. 72, no. 6, pp. 539–546, 2018, doi: 10.18926/AMO/56370.
[28] D. E. Rumelhart, G. E. Hinton, and R. J. Williams, "Learning representations by back-propagating errors," *Nature*, vol. 323, no. 6088, pp. 533–536, Oct. 1986.
[29] Y. Song, L. Yue, Y. Wang, H. Di, F. Gao, S. Li, Y. Zhou, and D. Hua, "Research on BP network for retrieving extinction coefficient from mie scattering signal of LiDAR," *Measurement*, vol. 164, Nov. 2020, Art. no. 108028, doi: 10.1016/j.measurement.2020.108028.
[30] B. Sang, "Application of genetic algorithm and BP neural network in supply chain finance under information sharing," *J. Comput. Appl. Math.*, vol. 384, Mar. 2021, Art. no. 113170, doi: 10.1016/j.cam.2020.113170.

MENG JIAO CHI received the bachelor's degree from Qilu Normal University, China, in 2021. She is currently pursuing the master's degree with Yantai University. Her research interest includes optical fiber two-parameter sensors.

HONG JUAN YANG was born in Shandong, China, in 1989. She received the B.S. degree in optical information science and technology and the Ph.D. degree in ocean exploration technology from the Ocean University of China, Qingdao, in 2012 and 2017, respectively. She is currently a Lecturer with the School of Physics and Electronic Information, Yantai University. Her current research interests include optical fiber sensors, microstructure fiber fabrication, and ocean detection.

KUN SHAN YANG is currently pursuing the B.E. degree in the Internet of Things engineering with Yantai University. His current research interests include optical fiber intelligent sensing and micromechanical learning.

WEI ZHUN DONG is currently pursuing the bachelor's degree in electronic information science and technology with Yantai University. His current research interests include fiber optic intelligent sensing and micromechanical learning.

XIN WEI WANG is currently pursuing the bachelor's degree in the Internet of Things engineering with the School of Physics and Electronic Information, Yantai University. His research interest includes optical fiber speckle sensors.

SEN ZHANG is currently pursuing the bachelor's degree in applied physics with Yantai University. His current research interest includes the study of liquid metals based on fiber optic structures.

XI CHANG WANG was born in July 1968. He received the degree from Changchun Institute of Optics and Fine Mechanics, Chinese Academy of Sciences, in 1999. He is currently with the School of Physics and Electronic Information Engineering, Yantai University. His research interest includes biomedical optics.

LING XIN KONG received the M.S. degree in measurement techniques and instruments from Northeast University and the Ph.D. degree in optical engineering from Nankai University.

He is currently with the School of Physics and Electronic Information Engineering, Yantai University. His research interests include optical fiber sensors and optical fiber-based micro-robots.